Estimation of Line Cross Sections Using Critical-Dimension Grazing-Incidence Small-Angle X-Ray Scattering

Guillaume Freychet,[1] Dinesh Kumar,[2,*] Ron J. Pandolfi,[2] Patrick Naulleau,[3] Isvar Cordova,[4,‡]
Peter Ercius,[5] Chengyu Song,[5] Joseph Strzalka,[6] and Alexander Hexemer[4,†]

[1] *NSLS-II, Brookhaven National Laboratory, Upton, NY 11973, USA*
[2] *Center for Advanced Mathematics for Energy Research Applications, Lawrence Berkeley National Laboratory, Berkeley, CA 94720, USA*
[3] *Center for X-ray Optics, Lawrence Berkeley National Laboratory, Berkeley, CA 94720, USA*
[4] *Advanced Light Source, Lawrence Berkeley National Laboratory, Berkeley, CA 94720, USA*
[5] *Molecular Foundary, Lawrence Berkeley National Laboratory, Berkeley, CA 94720, USA*
[6] *X-Ray Science Division, Advanced Photon Source, Argonne National Laboratory, Lemont, IL 60439, USA*

(Received 26 October 2018; revised manuscript received 16 July 2019; published 11 October 2019)

The semiconductor industry is continuously pushing the limits of photolithography, with feature sizes now smaller than 10 nm. To ensure quality, it has become necessary to look beyond the conventional metrological techniques. X-ray scattering has emerged as a possible contender to determine the average shape of a line grating with subnanometer precision. However, to fulfill its promise, faster algorithms must also be developed to interpret and extract metrics from reciprocal-space scattering data. In this paper, we present a fast and accurate x-ray technique and analysis algorithm: critical-dimension grazing-incidence small-angle x-ray scattering (CD GISAXS). The CD GISAXS technique is used in grazing-incidence configuration with a continuous azimuthal rotation of the sample, and thus does not require high-energy x-rays to penetrate the wafer and greatly reduces the data-acquisition times, permitting analysis within the framework of the distorted-wave Born approximation.

DOI: 10.1103/PhysRevApplied.12.044026

I. INTRODUCTION

Lithographically manufactured nanostructures continue to shrink in size in a struggle to keep pace with Moore's law. The semiconductor industry is exploring new metrology techniques capable of meeting the future requirement to characterize three-dimensional structures with sub-10-nm critical dimensions. Direct imaging techniques such as scanning electron microscopy and scanning force microscopy and indirect imaging techniques such as x-ray optical-critical-dimension scatterometry have been the state of the art when it comes to characterization of these structures [1–4]. All these approaches propose a way to probe nano-objects in depth, but are either approaching their resolution limits or are too slow for in-line measurements.

Therefore, the semiconductor industry is looking to supplement the metrology techniques. Several promising alternatives were listed in the International Technology Roadmap for Semiconductors [5]. One of them is the x-ray-scattering technique. Combined with the advent of high-brightness sources, faster detectors, and advances in mathematical treatment of scattering data, there is a real possibility of combining fast x-ray acquisition with high-speed data treatment to reach the timescales required for an effective in-line characterization method. One of the pioneering techniques, called critical-dimension small-angle x-ray scattering (CD SAXS), has been developed at the National Institute of Standards and Technology over the last few years and has demonstrated the ability of x-ray scattering to reconstruct line profiles with subnanometer resolution [6,7]. CD SAXS is a variable-angle transmission-scattering measurement where the sample is rotated to probe the vertical profile. The recent success of the use of iterative algorithms on CD SAXS data, more precisely a genetic algorithm coupled with a Monte Carlo Markov-chain approach, has led to precise reconstruction of the line profile's depth from a stack of trapezoids [8,9]. The approach has been extended to the study of polymer gratings and line-edge roughness [10–12].

Conducting such measurements in a transmission configuration imposes stringent requirements of high energy and high flux for the x rays to penetrate through silicon

---

[*] dkumar@lbl.gov

[†] ahexemer@lbl.gov

[‡] Also at Center for X-ray Optics, Lawrence Berkeley National Laboratory.

© 2019 American Physical Society

wafers, presenting a limitation of CD SAXS. It is a tough condition to meet, sometimes even for the modern state-of-the-art in-line sources. The attenuation through silicon substrates can require longer exposure times. However, applying this technique in combination with the use of reflection or “grazing-incidence” geometry can overcome this limitation of traditional CD SAXS; we present such a combined approach here.

Grazing-incidence small-angle x-ray scattering (GISAXS) is mostly used for the characterization of thin-film morphologies, but has recently been used to approximate the profile of polymer line gratings [13]. Precise alignment of the lines in the direction of the incoming beam is required to record a semicircle of spots, which are laid out as the intersection of the Ewald sphere with the Bragg rods from the gratings [14,15]. This allows the pitch of the gratings to be extracted from the position of the Bragg spots on the semicircle. To reconstruct the whole line profile, several approaches were developed. The first axis of development was the experimental one, aiming to collect more information from the line profile. To do so, Hoffman *et al*. [16] proposed rotating the gratings along the normal of the substrate to record the full Bragg rods. Later, Suh *et al*. [13] proposed recording GISAXS images at several incident angles to probe the form factor of the line profile across different regions of reciprocal space. In parallel, development improving data analysis progressed. Transmission scattering in grazing-incidence geometry, called GT-SAXS, was studied to get rid of the complexity of the distorted-wave Born approximation (DWBA) formalism [17]. A three-dimensional reconstruction of the line profile in the frame of the DWBA was proposed by Soltwisch *et al.* [18] by solving the Maxwell equations using finite elements. Most recently, Suh *et al.* [13] proposed a model to extract the roughness of line gratings with a combination of atomic force microscopy and GISAXS.

Here we extend the GISAXS approach proposed by Hoffman *et al.* [16], with a continuous rotation of the sample stage, to fit the form factor along several full Bragg rods—a more-holistic approach. The robustness of the fit is thus improved by increasing the number of experimental data points. The development of a genetic algorithm leads to the reconstruction of the line profile as a stack of trapezoids with subnanometer resolution [19,20]. The extracted line profile is then compared with cross-section TEM results.

II. CD GISAXS MEASUREMENTS

A. Sample preparation

CD GISAXS measurements are performed on 300-mm wafer samples provided by a leading semiconductor manufacturer and exposed on an ASML 193 immersion tool. The lines are made of resist with a nominal pitch of 87.6 nm. The patterned area is 10×20 mm^2.

B. Cross-section TEM

The focused-ion-beam (FIB) *ex situ* lift-out procedure [21] is used to extract cross-section specimens of the line patterns for characterization by scanning transmission electron microscopy (STEM). We use a Thermo Fischer Helios G4 operated by the National Center for Electron Microscopy facility of the Molecular Foundry. First, a layer of Pt is deposited with the electron beam onto the resist gratings to protect the exposed resist from the Ga$^+$-ion beam. Then, a second, thicker layer of Pt is deposited with the ion beam. The resulting sample lamella is attached to a Cu grid for further thinning to electron transparency with a 1-kV Ga$^+$ beam to remove FIB damage. High-resolution images of the cross-sectioned sample are then acquired with the National Center for Electron Microscopy’s Thermo Fischer Themis 60-300 operated in STEM mode. The images are acquired with a high-angle annular dark-field detector, 300-kV accelerating voltage, 10-mrad convergence angle, and 15-pA beam current.

C. CD GISAXS

CD GISAXS experiments are performed at beamline 8-ID-E of the Advanced Photon Source. A Pilatus 1M is positioned 2.19 m from the sample and the beamline energy is set at 10.915 keV. The incident angle is set at 0.16°, between the critical angles of silicon (0.165°) and the resist (0.12°). The 10×5 mm^2 etched pattern is mounted at the center of rotation of the beamline spin coater [22] such that the incoming beam is incident on the plane of the etched lines at 0.16°. Samples are rotated about the axis normal to the substrate as illustrated in Fig. 1. The footprint of the beam is several centimeters, and thus the whole etched area is illuminated during the measurement. The wobbling effect introduced by the rotation of the spin coater is quantified on the beamline by our comparing results between two x-ray reflectivity measurements of a polymer thin-film sample performed under static and rotation configurations. The results show a slight broadening of the Kiessig fringes, but the broadening effect on the FWHM is contained to below 5%.

The Fourier rods coming from the gratings, also known as Bragg rods, intersect with the momentum-transfer vector of the elastic x-ray scattering at a single point above the horizon. The Bragg rods can be scanned by rotating the momentum-transfer vector, and therefore the sample. The GISAXS image, shown in Fig. 2, is recorded with an acquisition time of 100 s with the sample rotating at 500 revolutions/min during the acquisition. The experimental data are remeshed into the reciprocal space, explaining the absence of data at $q_{\parallel} = 0$ nm^{-1}. The intensity of the recorded Bragg rods is modulated by the Fourier transform of the shape (i.e., the form factor of the individual grating

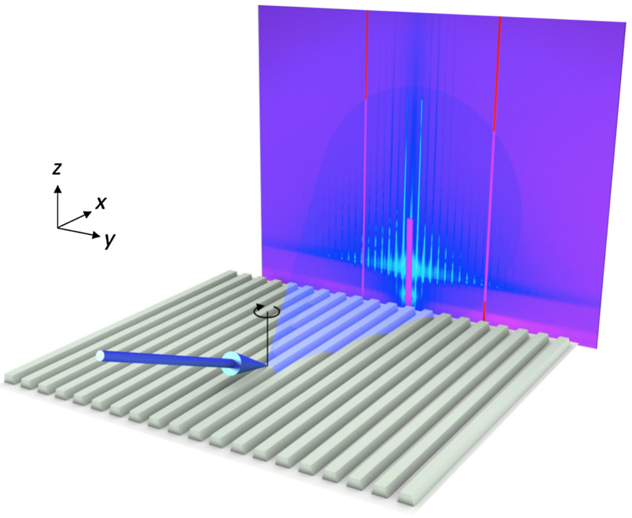

FIG. 1. Grazing-incidence small-angle x-ray scattering with the beam along the x axis and the sample rotation along the z axis.

lines is visible with line-cuts along the Bragg rods). Each profile is indexed and shown in Fig. 2(b). Therefore, as for diblock copolymers, these modulations provide depth information, and more precisely come from the cross-section of the line [23]. Moreover, the full rotation of the sample, 360°, overcomes the need for precise alignment of the line with regard to the beam. In the absence of the aforementioned setup, a subdegree alignment is needed for GISAXS measurements.

III. THEORY

In this section we discuss the theoretical model used in simulation of the form factor and subsequent reconstruction of the line shapes. The DWBA is commonly used in the modeling of grazing-incidence scattering events. The sample is approximated as a ridge repeated at regular intervals in a one-dimensional lattice, so scattering gets you the form factor of the ridge sampled by the structure factor from the lattice, and we observe the intersection of this with the idealized Ewald sphere projected onto the plane of the detector, resulting in small spots arranged in a semicircle when the ridges are parallel to the beam [13]. When the sample is rotated *in plane* during the GISAXS measurement, these spots move along the z axis, while staying stationary along the y axis, in reciprocal space. The final scattering image contains high-intensity continuous vertical lines. These lines are modulated by the form factor. Assuming that the line shape does not vary significantly, we can simulate these vertical lines using the DWBA. A similar pattern can be achieved by continuously changing the angle of the incident beam, but this increases the complexity of the algorithm, because the coordinate values change for every change in the incident angle [Eq. (1)].

$$\begin{Bmatrix} q_x \\ q_y \\ q_z \end{Bmatrix} = \frac{2\pi}{\lambda} \begin{pmatrix} \cos\alpha\cos\theta - \cos\alpha_i \\ \cos\alpha\sin\theta \\ \sin\alpha + \sin\alpha_i \end{pmatrix}. \tag{1}$$

The simulations for all the incident angles in the range need to be in the detector coordinate system before they can be added to and compared with the scattering data.

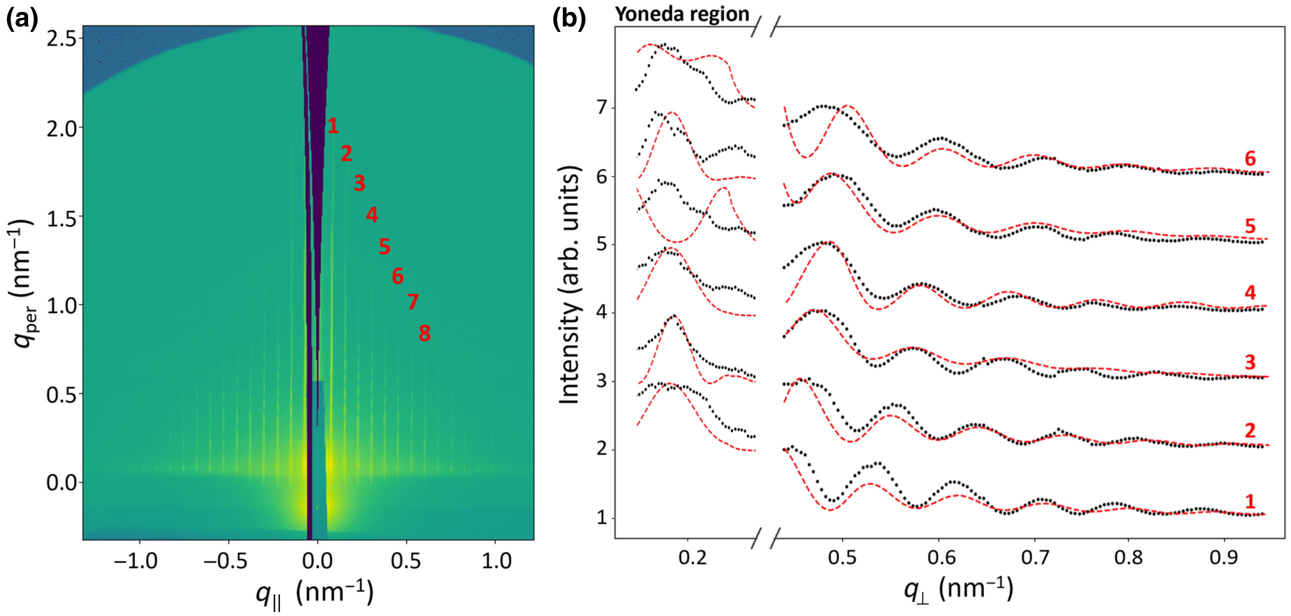

FIG. 2. (a) CD GISAXS images recorded with a rotation of the gratings under the beam and (b) the corresponding $q_{\perp}$ profiles obtained from one-dimensional cuts along the Bragg rods.

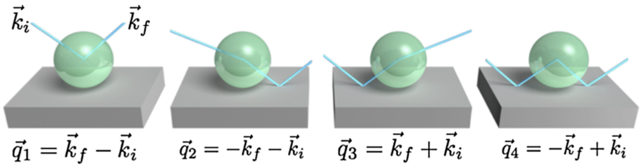

FIG. 3. Four terms involved in the scattering in the frame of the DWBA. The first term corresponds to the simple Born approximation. The higher-order terms reflect the impact events at the silicon-substrate interface.

A. DWBA

The DWBA extends the Born approximation to include both reflective and refractive events to compute the scattering. Under the assumptions of stratified media, Maxwell's electromagnetic equations can be reduced to Helmholtz's equations. The resulting homogeneous equations can be solved exactly with use of a Green's function. Instead of deriving the DWBA, we refer the reader to Refs. [24,25] for a detailed discussion of the topic. Similarly to the Born approximation, where detector intensity is proportional to the absolute squared value of the Fourier transform of the electron density of the scatterer, the DWBA stipulates that intensity is proportional to the absolute squared value of the summation of four scattering events; see Fig. 3 and Eq. (2):

$$I(q_\parallel, q_\perp) \propto \left|\mathcal{F}(q_\parallel, q_\perp)\right|^2, \tag{2}$$

$$\mathcal{F}_i(q_\parallel, q_\perp) = \sum_{j=1}^{4} C_i\,(\alpha^f, \alpha^i; \eta, t) F_i\left(q_x, q_y, \pm k_z^f \mp k_z^i; \ell\right), \tag{3}$$

where C_i is the Fresnel coefficient for a given medium with complex refractive index η and thickness t, F_i is the Fourier transform of a shape with dimensions ℓ, and $q_\parallel$ and $q_\perp$ have their usual meaning. If the medium is air (or a vacuum), that is, $\eta = 0$, the calculation Fresnel coefficient is simplified to

$$C = [1, r(\alpha^i), r(\alpha^f), r(\alpha^i) r(\alpha^f)]^T,$$

$$r = \frac{k_z - \tilde{k}_z}{k_z + \tilde{k}_z},$$

$$\tilde{k}_z = -\sqrt{\eta_s^2 k_0^2 - |k_\parallel|^2},$$

where η_s is the complex refractive index of the substrate.

There are software tools, such as HipGISAXS, BornAgain, and IsGISAXS, to calculate GISAXS patterns [26,27].

B. Simulation of the form factor

If we assume that the etched line gratings are infinitely long, the mathematical problem of resolving the shape of the gratings is reduced to a two-dimensional cross section. The cross section of line gratings can be approximated by stacking multiple trapezoids. To simplify the description of the line profile, the trapezoids' heights, h, are kept identical for each trapezoid. Moreover, each trapezoid is symmetric, with both of its sidewall angles equal. Each trapezoid is therefore described by a sidewall angle β, a height h, and a bottom width L, as illustrated in Fig. 4. The Fourier transform of each trapezoid can be expressed as

$$F(q_y, q_z) = \frac{1}{q_y}\left[-m e^{jh(q_y L/2)}\left(1 - e^{-jh[(q_y + m\,q_z)/m]}\right) + m e^{-jh(q_y L/2)}\left(1 - e^{-jh[(q_y + m\,q_z)/m]}\right)\right],$$

where m is the tangent of the sidewall angle. The Fourier transform of the tessellation is given by

$$\mathcal{F} = \sum_{n=0}^{N} \mathcal{F}_n e^{j\,h\,n\,q_z}, \tag{4}$$

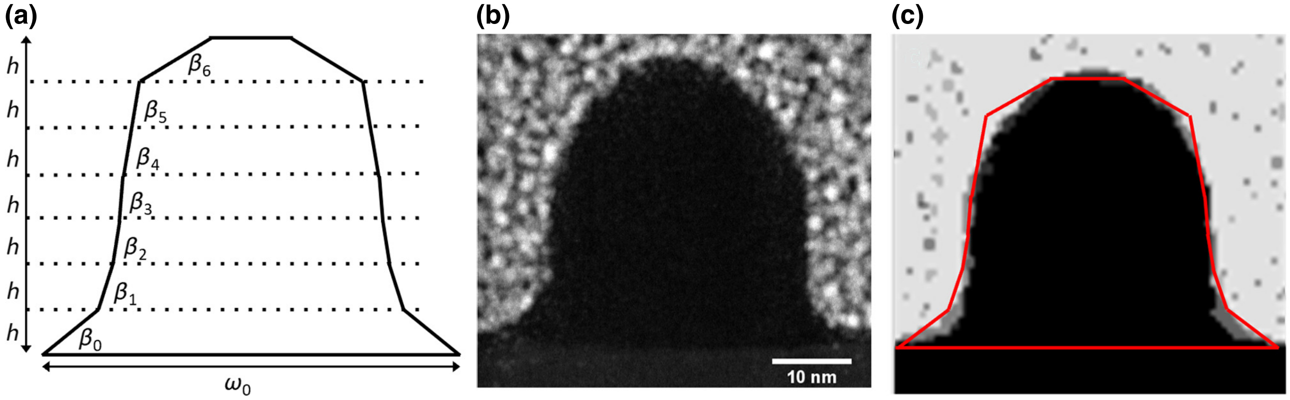

FIG. 4. (a) The line profile determined by CD GISAXS can be compared with (b) the annular dark-field image extracted from cross-section STEM and (c) a direct comparison between the CD GISAXS and three averaged cross-section-STEM profiles.

where $\mathcal{F}_n$ is the Fourier transform of the nth trapezoid.

Since the bottom line width of each trapezoid is calculated from the top line width of the trapezoid under it, the tessellation of trapezoids can be described with $N+2$ parameters: the trapezoids' heights, h; a sidewall angle per trapezoid; and the bottom width of the trapezoid underneath.

As illustrated in Fig. 4(a), the line profile is modeled with $N = 7$, a reasonable compromise between the accuracy of the model and the computational time. Comparison with the cross-section-STEM image shown in Fig. 4(b) reveals our model realistically reproduces the overall line profile. To account for interfacial roughness, a Debye-Waller factor is also given as an initial parameter for the fitting procedure. This brings the number of initial parameters to ten (nine for a stack of seven trapezoids and the Debye-Waller factor).

C. Genetic algorithm

From the previous section, we can simulate the modulations recorded on the Bragg rods in the context of the DWBA. From there, we apply a strategy similar to the one developed by Hannon *et al.* [9] for CD SAXS.

The approach is based on a genetic and evolutionary algorithm, showing good convergence performance on large parameter spaces. Such algorithms mimic biological evolution using the model parameter sets as the encoding genetic information. Genetic algorithms usually start with a population of candidate solutions. This population goes through *mutation* by exchanging the parameters within the population. This is followed by *selection*. The most-suitable offsprings resulting from the mutation are selected for the next generation. The process is repeated until the desired goodness of fit is achieved. Several algorithms were tested by Hannon *et al.* [9], and the covariance-matrix-adaptation evolutionary strategy (CMAES) was the best compromise between efficiency and reliability. This approach is intended to reduce the number of generations and therefore the convergence efficiency. In our procedure, the population size is fixed to 100, significantly greater than the lower bound optimal for ten parameters. Such a large population size is desired to improve the global-search properties and also the implementation of the parallelization of the strategy, which is the target of future work. A mutational rate of 10, meaning ten individuals mixed in each generation, is used in the determination of the further evolutionary strategy.

With the CMAES approach, fitting ten variable parameters converges in 120 s. The best extracted profile is displayed in Fig. 4(a). The robustness of convergence is tested by our performing the CMAES approach with several randomized initial model parameters; all converged to the same profile.

IV. RESULTS AND DISCUSSION

The best line profile extracted by CD GISAXS is presented in Fig. 4(a), corresponding to the fit presented in Fig. 2(b). The height of each trapezoid h is 5.1 nm, leading to an overall line height of 35.84 nm and the bottom line width ω_0 is 49.8 nm. A cross-section-TEM measurement is done to get a direct image of the line profile and validate the model extracted by CD GISAXS (Table I).

The overall profiles extracted by CD GISAXS and cross-section STEM present similarities such as the presence of a footing (i.e., a wider width at the bottom of the line at the substrate interface) and the presence of a rounding effect at the top of the line. Both of these aspects of the line shape are common for a grating generated by electron-beam lithography [7]. However, although the overall profile extracted by CD GISAXS is quite similar to the STEM image, closer inspection reveals some mismatches. These mismatches can be attributed partly to our definition of the line profile. One of our first assumptions was the symmetry of the trapezoids, which seems to be incorrect with respect to the STEM image. Moreover, a stack of seven trapezoids cannot describe such a smooth rounding effect at the top of the line. However, seven trapezoids seems to be the limit at which increasing the number of trapezoids dos not improve the fit anymore and leads to oversampling the line profile Fig. 5.

However, even though cross-section STEM gave us a good estimate of the line profile, a direct comparison between a single line profile and the profile averaged over several square millimeters leads to another source of error. Indeed, the dispersion of the line profile, present in the sample and illustrated in the cross-section-scanning-electron-microscopy image in Fig. 6, will impact the CD GISAXS data, specifically the Yoneda area, which is sensitive to the in-depth variation of the electronic density gradient. Our current simulation of a monodisperse line profile leads to two intense and sharp Yoneda peaks, characteristic of the electronic density of the silicon substrate and the average density of the line grating. This is not representative of the experimental data, which present a

TABLE I. Comparison of the parameters of the line profile determined by CD GISAXS and cross-section STEM.

	ω_0 (nm)	h (nm)	β_0 (deg)	β_1 (deg)	β_2 (deg)	β_3 (deg)	β_4 (deg)	β_5 (deg)	β_6 (deg)
STEM	50.2	5.1	48	74	93	86	82	66	45
CD GISAXS	49.8	5.1	48	74	84	87	82	81	34

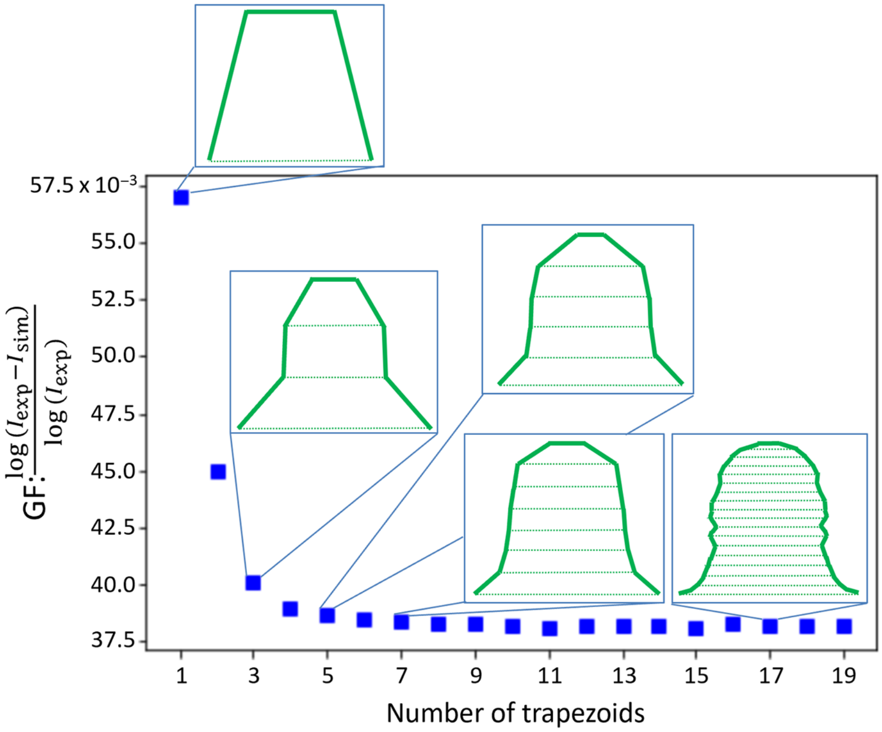

FIG. 5. Evolution of the goodness of the fit (GF) with model complexity.

blurring of Yoneda peaks, characteristic of a dispersion of the profile. Also, the two distinct Yoneda peaks in the experimental data are not observed even in the static GISAXS, and thus this is not a result of instability in the air bearing.

The counts in the Yoneda region may be under-reported. This could be due to the count rate exceeding the linear counting regime of the Pilatus detector (less than 10^6 counts/s). The counters are reset after the threshold is reached. Silicon gratings, for all their imperfections, produce very strong Bragg scattering, especially so in the Yoneda region. Such mismatch between our model and the experimental data leads us to crop or exclude the Yoneda area, $q_{\perp} \in [0, 0.4]\,\mathrm{nm}^{-1}$ to allow the convergence of the fit, as illustrated in Fig. 2(b).

Nevertheless, even though the Yoneda area is not considered for the fit, the region $0.4\ \mathrm{nm}^{-1} \leq q_{\perp} \leq 0.5\ \mathrm{nm}^{-1}$ is still not satisfactorily reproduced. This is a residual contribution from the Yoneda area. Therefore, to improve the fit, a dispersion of the line profile needs to be added and is the target of our future work. Furthermore, a Monte Carlo Markov-chain algorithm is under development to provide an uncertainty quantification of the extracted profile.

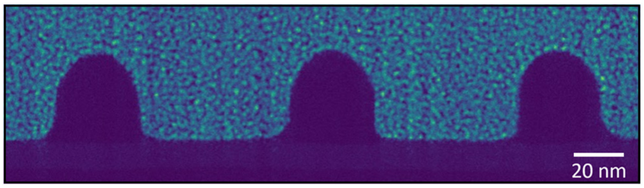

FIG. 6. Cross-section-STEM image revealing dispersion of the line profile.

V. CONCLUSION

The reconstruction of the profile of line gratings is performed by small-angle x-ray scattering under a grazing-incidence geometry. The consistency with cross-section STEM leads to some confidence in the ability of CDGISAXS to recreate the line profile. Results such as this open alternative perspectives on the x-ray-scattering techniques to be used as a metrology tool by the semiconductor industry. The main novelty brought by the reflection geometry is the possibility to perform CD GISAXS with every x-ray energy or wavelength. Therefore, Cu $K\alpha$ sources and compact x-ray sources operating below 15 keV—otherwise irrelevant for traditional CD SAXS since the transmission through the wafer is not sufficient—can be used.

The short acquisition time of CD GISAXS could potentially allow this technique to reach a throughput targeted by the semiconductor industry, even though the beam footprint needs to be reduced to be completely viable for such applications. Additional algorithms for line-profile modeling need to be developed to introduce dispersion of the line profile and therefore a more-realistic description of the sample.

ACKNOWLEDGMENTS

We acknowledge support from the LBNL LDRD program, the DOE Early Career Award program, and the

Center for Advanced Mathematics in Energy Research Applications, funded jointly through the ASCR and BES programs of the U.S. Department of Energy (DOE). This work used resources of the U.S. DOE Office of Science User Facilities, supported under Contracts No. DE-AC02-98CH10886 (National Synchrotron Light Source II, Brookhaven National Laboratory) and No. DE-AC02-06CH11357 (Advanced Photon Source, Argonne National Laboratory). Experiments performed at the Molecular Foundry, Lawrence Berkeley National Laboratory, were supported by the U.S. DOE under Contract No. DE-AC02-05CH11231. We thank John Turner of the Molecular Foundry for support with the preparation of the FIB cross-sectioned sample. We also thank Ruipeng Li for helping tremendously with early CD GISAXS measurements at the CMS beamline at National Synchrotron Light Source II.

[1] R. Silver, T. Germer, R. Attota, M. B. Barnes, B. Bunday, J. Allgair, E. Marx, and J. Jun, Fundamental limits of optical critical dimension metrology: A simulation study, Proc. SPIE **6518**, 65180U (2007).

[2] B. D. Bunday, T. A. Germer, V. Vartanian, A. Cordes, A. Cepler, and C. Settens, Gaps analysis for cd metrology beyond the 22 nm node, Proc. SPIE **8681**, 8681 (2013).

[3] B. D. Bunday, D. K. Michelson, J. A. Allgair, A. Tam, D. Chase-Colin, A. Dajczman, O. Adan, and M. Har-Zvi, CD sem metrology macro CD technology: Beyond the average, Proc. SPIE **5752**, 5752 (2005).

[4] K. Ueda, T. Mizuno, and K. Setoguchi, High accuracy CD matching monitor for CD-SEM beyond 20 nm process, Proc. SPIE **8681**, 8681 (2013).

[5] International technology roadmap for semiconductors (2013).

[6] R. L. Jones, T. Hu, E. K. Lin, W.-L. Wu, R. Kolb, D. M. Casa, P. J. Bolton, and G. G. Barclay, Small angle x-ray scattering for sub-100 nm pattern characterization, Appl. Phys. Lett. **83**, 4059 (2003).

[7] D. F. Sunday, M. R. Hammond, C. Wang, W.-L. Wu, R. J. Kline, and G. E. Stein, Three-dimensional x-ray metrology for block copolymer lithography line-space patterns, J. Micro. Nanolithogr. MEMS MOEMS **12**, 12 (2013).

[8] D. F. Sunday, E. Ashley, L. Wan, K. C. Patel, R. Ruiz, and R. J. Kline, Template–polymer commensurability and directed self-assembly block copolymer lithography, J. Polym. Sci. Pol. Phys. **53**, 595 (2015).

[9] A. F. Hannon, D. F. Sunday, D. Windover, and R. J. Kline, Advancing x-ray scattering metrology using inverse genetic algorithms, J. Micro. Nanolithogr. MEMS MOEMS **15**, 15 (2016).

[10] D. F. Sunday, S. List, J. S. Chawla, and R. J. Kline, Determining the shape and periodicity of nanostructures using small-angle x-ray scattering, J. Appl. Crystallogr. **48**, 1355 (2015).

[11] G. Freychet, C. Cadoux, Y. Blancquaert, S. Rey, M. Maret, and P. Gergaud, A study of lateral roughness evaluation through critical-dimension small angle x-ray scattering (CD-SAXS), Proc. SPIE **9778**, 9778 (2016).

[12] J. Reche, M. Besacier, P. Gergaud, Y. Blancquaert, G. Freychet, and T. Labbaye, Programmed LWR metrology by multi-techniques approach, Proc. SPIE **10585**, 10585 (2018).

[13] H. S. Suh, X. Chen, P. A. Rincon-Delgadillo, Z. Jiang, J. Strzalka, J. Wang, W. Chen, R. Gronheid, J. J. D. Pablo, N. Ferrier, M. Doxastakis, and P. Nealey, Characterization of the shape and line-edge roughness of polymer gratings with grazing incidence small-angle x-ray scattering and atomic force microscopy, J. Appl. Crystallogr. **49**, 823 (2016).

[14] P. Mikulik, M. Jergel, T. Baumbach, E. Majkova, E. Pincik, S. Luby, L. Ortega, R. Tucoulou, P. Hudek, and I. Kostic, Coplanar and non-coplanar x-ray reflectivity characterization of lateral W/Si multilayer gratings, J. Phys. D: Appl. Phys. **34**, A188 (2001).

[15] M. Yan and A. Gibaud, On the intersection of grating truncation rods with the ewald sphere studied by grazing-incidence small-angle x-ray scattering, J. Appl. Crystallogr. **40**, 1050 (2007).

[16] T. Hofmann, E. Dobisz, and B. M. Ocko, Grazing incident small angle x-ray scattering: A metrology to probe nanopatterned surfaces, J. Vac. Sci. Technol. B Microelectron. Nanometer. Struct. Process. Meas. Phenom. **27**, 3238 (2009).

[17] X. Lu, K. G. Yager, D. Johnston, C. T. Black, and B. M. Ocko, Grazing-incidence transmission x-ray scattering: Surface scattering in the born approximation, J. Appl. Crystallogr. **46**, 165 (2013).

[18] V. Soltwisch, J. Wernecke, A. Haase, J. Probstand, M. Schoengen, M. Krumrey, and F. Scholze, Nanometrology on gratings with GISAXS: FEM reconstruction and fourier analysis, Proc. SPIE **9050**, 9050 (2014).

[19] G. Freychet, D. Kumar, R. Pandolfi, D. Staacks, P. Naulleau, R. J. Kline, D. Sunday, M. Fukuto, J. Strzalka, and A. Hexemer, Critical-dimension grazing incidence small angle x-ray scattering, Proc. SPIE **10585**, 10585 (2018).

[20] G. Freychet, I. A. Cordova, T. McAfee, D. Kumar, R. J. Pandolfi, C. Anderson, S. D. Dhuey, P. Naulleau, C. Wang, and A. Hexemer, Reconstructing the three-dimensional latent image of extreme ultraviolet resists with resonant soft x-ray scattering, J. Micro. Nanolithogr. MEMS MOEMS **18**, 1 (2019).

[21] L. A. Giannuzzi and F. A. Stevie, eds., *Introduction to Focused Ion Beams: Instrumentation, Theory, Techniques and Practice* (Springer, 2005).

[22] E. F. Manley, J. Strzalka, T. J. Fauvell, N. E. Jackson, M. J. Leonardi, N. D. Eastham, T. J. Marks, and L. X. Chen, In situ GIWAXS analysis of solvent and additive effects on PTB7 thin film microstructure evolution during spin coating, Adv. Mater. **29**, A129 (2017).

[23] G. Freychet, M. Maret, R. Tiron, X. Chevalier, A. Gharbi, M. Fernandez-Regulez, and P. Gergaud, Removal of poly(methyl methacrylate) in diblock copolymers films studied by grazing incidence small-angle x-ray scattering, J. Polym. Sci. Pol. Phys. **54**, 1137 (2016).

[24] S. K. Sinha, E. B. Sirota, S. Garoff, and H. B. Stanley, X-ray and neutron scattering from rough surfaces, Phys. Rev. B **38**, 2297 (1988).

[25] G. Renaud, R. Lazzari, and F. Leroy, Probing surface and interface morphology with grazing incidence small angle x-ray scattering, Sur. Sci. Rep. **64**, 255 (2009).

[26] R. Lazzari, *IsGISAXS*: A program for grazing-incidence small-angle x-ray scattering analysis of supported islands, J. Appl. Crystallogr. **35**, 406 (2002).

[27] S. T. Chourou, A. Sarje, X. S. Li, E. R. Chan, and A. Hexemer, *HipGISAXS*: A high-performance computing code for simulating grazing-incidence x-ray scattering data, J. Appl. Crystallogr. **46**, 1781 (2013).